ACS NANO

www.acsnano.org

ARTICLE

Engineering Chalcogenide-Containing Spacers: Modulating Internal Interactions for Enhanced Performance and Stability in Ruddlesden–Popper Perovskite Devices

Yi Shen, Zhengxun Lai,* Siliang Hu, Boxiang Gao, Yan Yan, Haifan Li, Shiyan Shan, Jianbo Wu, Dong Chen, Yuxuan Zhang, Dylan Xiangyu Fan, Chun-Yuen Wong, and Johnny C. Ho*

Cite This: *ACS Nano* 2025, 19, 41498–41508

Read Online

ACCESS | Metrics & More | Article Recommendations | Supporting Information

ABSTRACT: Two-dimensional (2D) Ruddlesden–Popper (RP) halide perovskites are promising for optoelectronic applications due to their enhanced stability compared to 3D versions. However, their practical application is still hindered by the inherent instability arising from weak interactions between adjacent organic layers. To address this challenge, we engineered 2D RP perovskites using four organic spacers: 3-thiophene-methylammonium (3-TMA) and 3-furan-methylammonium (3-FMA), with 2-thiophene-methylammonium (2-TMA) and 2-furan-methylammonium (2-FMA) as controls. Our findings highlight that the heteroatom type (S vs O) and spacer regiochemistry significantly influence interaction strength. Thiophene-based spacers bond more robustly to inorganic layers than furan-based ones. Notably, shifting the thiophene spacer configuration from 2-TMA to 3-TMA markedly strengthens interactions between organic layers, improving RP perovskite stability under ambient and thermal conditions. Utilizing the substantial dipole moment of the optimized 3-TMA spacer, we developed an enhanced performance perovskite photodetector with a responsivity of 153 mA/W and detectivity of 1.7×10^{10} Jones. This study offers insights into RP perovskite stability and guides the design of durable perovskite devices through strategic spacer engineering.

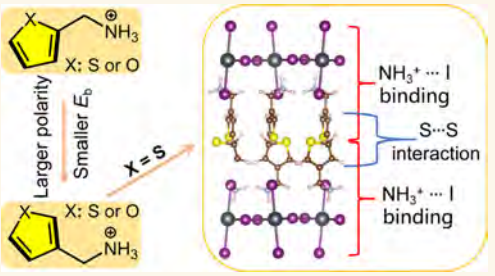

KEYWORDS: *halide perovskite, aromatic spacer, interaction, photodetector, stability*

INTRODUCTION

In recent years, academic research and commercial ventures have highlighted the vast potential of halide perovskites in photovoltaic devices, driven by their good optoelectronic properties.[1−4] Perovskite-based devices, including solar cells,[5,6] light-emitting diodes,[7,8] detectors,[9−13] and transistors,[14−16] have made significant strides. However, their long-term stability under standard conditions remains a major challenge.[17−19] To tackle this, incorporating large organic spacer cations into 3D perovskites has proven effective in enhancing stability.[20] Traditionally, 3D perovskites follow the formula ABX_3, where A is Cs^+, $CH(NH)NH_3^+$, or $CH_3NH_3^+$; B is a divalent metal ion (Pb^{2+} or Sn^{2+}); and X is a halide ion (I^-, Br^-, or Cl^-). In contrast, 2D Ruddlesden–Popper (RP) perovskites are formed by the alternating arrangement of organic spacer and inorganic octahedral layers. This structure grants 2D RP perovskites superior moisture, thermal and light stability compared to their 3D counterparts.[21,22] The bonding in RP perovskites is maintained by hydrogen bonds and van der Waals forces, with the general formula $R_2A_{n-1}B_nX_{3n+1}$, where R is a monovalent spacer cation, n denotes the number of BX_6 octahedral layers, and A, B, and X are the same as in 3D perovskites.

The organic ammonium ion layers in 2D RP perovskites provide greater flexibility than 3D perovskites, enhancing their optoelectronic properties and stability, and expanding their applications. Specifically, the organic layers affect RP perovskites by (1) inducing quantum and dielectric confinement effects due to their lower dielectric constant, thus increasing exciton binding energy;[23,24] (2) interacting with BX_6 octahedra, distorting the lattice, and affecting performance and stability;[25,26] and (3) influencing properties and stability through Coulomb inter-

Received: June 1, 2025
Revised: November 23, 2025
Accepted: November 24, 2025
Published: December 1, 2025

https://doi.org/10.1021/acsnano.5c09104
ACS Nano 2025, 19, 41498–41508

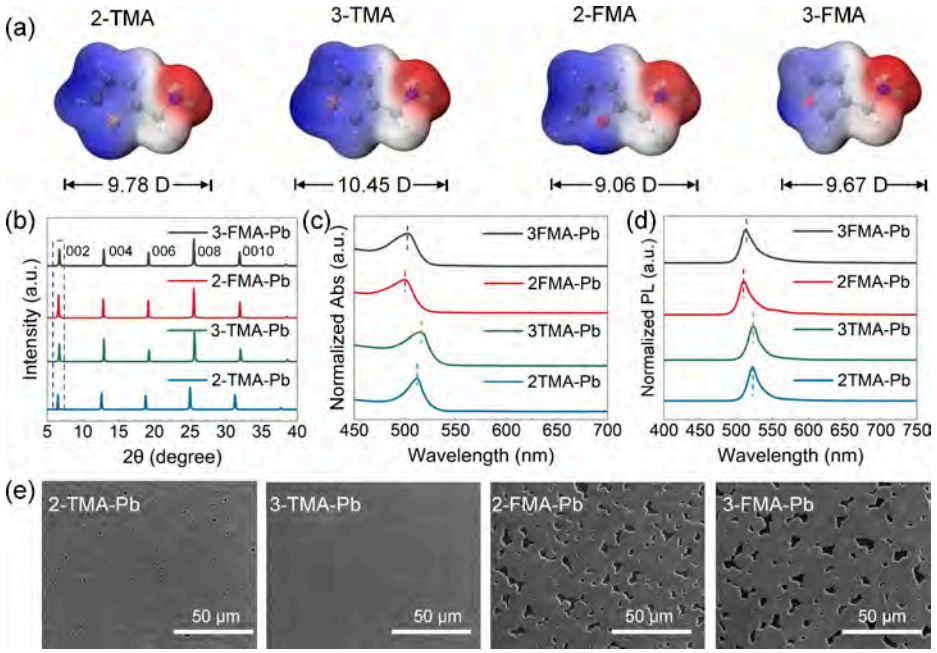

Figure 1. (a) Chemical structure, ESP, and dipole moment for 2-TMA, 3-TMA, 2-FMA, and 3-FMA spacers. (b) XRD patterns of 2-TMA-Pb, 3-TMA-Pb, 2-FMA-Pb, and 3-FMA-Pb perovskite films. (c) UV−vis absorption spectra of these films. (d) PL spectra of these films. (e) SEM images of these films.

actions, including stacking arrangements, heteroatomic interactions, and $\pi-\pi$ effects.[27]

Extensive efforts have focused on optimizing perovskite materials' structural and electronic properties through the strategic design and application of tailored spacers. Spacers with large dipole moments have notably mitigated quantum and dielectric confinement effects, enhancing exciton separation and transport.[28] Examples include 4-fluoro-phene-ethylammonium (4F-PEA),[29,30] 2-fluoro-2-phenylethan-1-aminium (β-FPEA),[31] and 2-thiophene-ethylammonium (2-TEA),[32] which improves overall perovskite stability by interacting favorably with the BX_6 layers.

Recently, interlayer interaction in RP perovskites has drawn increasing attention. For instance, Ren et al. demonstrated that sulfur atoms at the terminal position of the butylamine (BA) spacer enhance perovskite film quality and stability through strong S···S interactions.[27] Similarly, Li et al. showed that fluorine atoms in FPEA cations stabilize the perovskite structure via supramolecular electrostatic interactions.[33] Despite the progress, the development of spacer cations capable of effectively enhancing interlayer interactions in RP perovskites remains limited, particularly in aromatic spacers. These spacers inherently offer several advantages, including higher dielectric constants, greater rigidity, superior structural tunability, and the ability to induce perpendicular growth of quasi-2D perovskite lattices.[34]

Chalcogen-containing aromatic rings, which possess lone pair electrons, have been explored as spacers in RP perovskites, such as 2-thiophene-methylammonium (2-TMA),[35,36] 2-furan-methylammonium (2-FMA),[37,38] and 2-selenophene-methylammonium (2-SeMA).[39] These spacers interact strongly with inorganic BX_6 octahedra, stabilizing RP perovskite structures. However, their potential to enhance organic layer-to-layer interactions remains largely unexplored. Given their great electronic properties and structural versatility, such spacers hold promise for regulating internal interactions in RP perovskites, improving material stability and performance.

In this study, we provided a systematic comparative study where Pb-based 2D perovskites using 3-TMA_2PbI_4 and 3-FMA_2PbI_4 (3-TMA = 3-thiophene-methylammonium and 3-FMA = 3-furan-methylammonium) were synthesized, alongside 2-TMA_2PbI_4 and 2-FMA_2PbI_4 as reference materials. Our findings reveal that altering the spacer configuration from 2- to 3-position significantly increases the polarity of perovskite structures. The heteroatom type and position within the spacer profoundly influence interactions between organic layers and both inorganic PbX_6 sheets and adjacent organic layers. Notably, thiophene-based spacers exhibit stronger interactions with inorganic layers than furan-based spacers, and the repositioning of the sulfur atom (from position 2 to position 3) effectively shortens the S···S distance between adjacent organic layers, facilitating strong S···S interactions and enhancing stacking stability. Consequently, the 3-TMA_2PbI_4 perovskite film demonstrates the highest stability among these perovskites under various environmental conditions, including air, heat, and light. Furthermore, the large dipole moment of the 3-TMA spacer enables the development of an enhanced performance perovskite photodetector, achieving a best responsivity of 153 mA/W and detectivity of 1.7×10^{10} Jones among these detectors. These results deepen our understanding of chalcogenide atom interaction in RP perovskites and provide valuable insights for designing high-performance, stable perovskite materials.

RESULTS AND DISCUSSION

As is well-established, heteroatoms—primarily chalcogenides (*e.g.*, S and Se) and halogens (*e.g.*, Cl, Br, and I)—play a pivotal role in modulating the internal interactions within RP perovskites. To systematically investigate the influence of chalcogenide heteroatoms on these interactions, we designed and synthesized a series of aromatic spacer cations incorporating

https://doi.org/10.1021/acsnano.5c09104
ACS Nano 2025, 19, 41498−41508

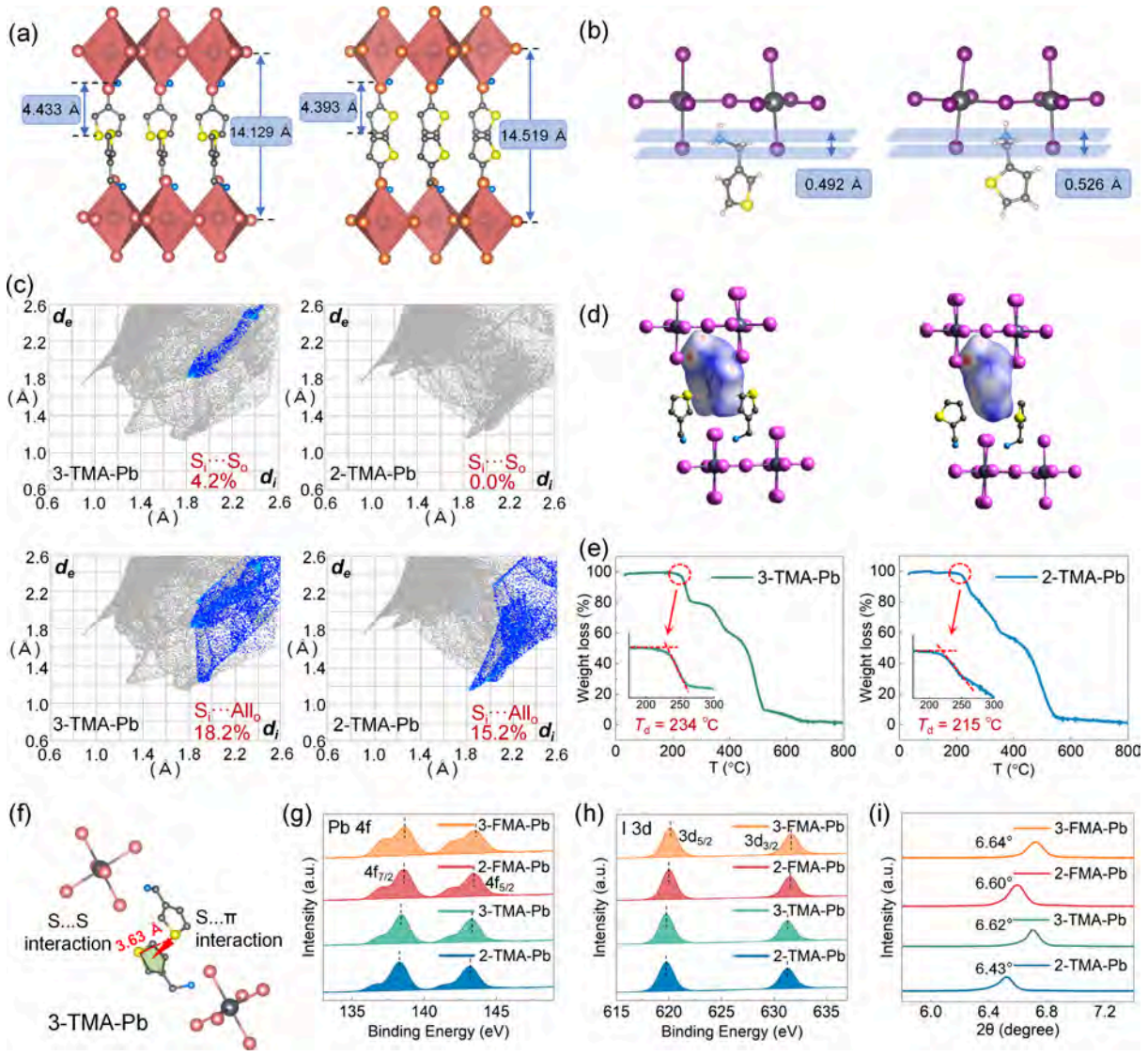

Figure 2. (a) Single-crystal structures of 3-TMA-Pb (left) and 2-TMA-Pb (right) perovskites. The inorganic layer spacing and length of the spacer skeleton are illustrated. (b) Penetration depth d_p of 3-TMA-Pb (left) and 2-TMA-Pb (right) perovskites. (c, d) Hirschfeld surface analysis for interaction within 3-TMA-Pb (left) and 2-TMA-Pb (right) perovskites. (e) Results of TGA measurements for 3-TMA-Pb (left) and 2-TMA-Pb (right) crystals. (f) Schematic diagram for S···S interaction and S···π interaction in 3-TMA-Pb perovskite. (g) XPS spectra of Pb 4f and I 3d for 2-TMA-Pb, 3-TMA-Pb, 2-FMA-Pb, and 3-FMA-Pb perovskite films. (h) Magnified XRD view of the (002) peak for these perovskite films.

chalcogenide atoms: 2-TMA, 3-TMA, 2-FMA, and 3-FMA, as illustrated in Figure 1a (see Figures S1−S7 in the Supporting Information for details). These four spacers exhibit comparable molecular sizes and structural frameworks, thereby minimizing extraneous factors that could induce perovskite lattice distortions and enabling a more focused exploration of the internal interactions regulated by the chalcogenide heteroatoms. Furthermore, the positional variation of the heteroatoms is anticipated to fine-tune the internal interactions within the perovskite structure while simultaneously altering the polarity of the spacer cations. To quantitatively assess these effects, we first performed density functional theory (DFT) calculations to determine the dipole moments of the four spacer cations. As shown in Figure 1a, the dipole moments increase in the following order: 2-FMA (9.06 D), 3-FMA (9.67 D), 2-TMA (9.78 D), and 3-TMA (10.45 D). The enhanced dipole moment is closely associated with the increased polarity of the spacer layer, which is expected to mitigate quantum and dielectric confinement effects, thereby facilitating the separation and transport of excitons within the perovskite structure.[28,40] Moreover, we also calculated relaxed perovskite structures (n = 1) with these four spacers to investigate their band structures, and the results are shown in Figure S8 and Table S1 in the Supporting Information. We can see that the band gaps and structures reveal minimal variations across these RP perovskites. This consistency arises from the structurally analogous inorganic $[PbI_6]^{4-}$ frameworks induced by the incorporation of chemically similar spacers, which dominate the electronic band structure—a well-documented characteristic of low-dimensional perovskites where inorganic sublattices primarily govern optoelectronic properties.

Subsequently, we synthesized four RP perovskite films with n = 1 using the aforementioned aromatic spacers: 2-TMA_2PbI_4, 3-TMA_2PbI_4, 2-FMA_2PbI_4, and 3-FMA_2PbI_4, hereafter referred to as 2-TMA-Pb, 3-TMA-Pb, 2-FMA-Pb, and 3-FMA-Pb, respectively. To confirm the formation of pure RP-phase

https://doi.org/10.1021/acsnano.5c09104
ACS Nano 2025, 19, 41498−41508

perovskite structures, these films were first characterized by X-ray diffraction (XRD). As shown in Figure 1b, all films exhibit strong and sharp XRD peaks, indicating the formation of 2D layered structures. By comparing with previously reported data, these peaks can be assigned to the (00n) lattice planes of layered perovskites, suggesting a highly ordered growth of the perovskite lattice. Such structural ordering is particularly advantageous for efficient carrier transport within the material. Notably, the full width at half-maximum (FWHM) of peaks of 2-TMA-Pb and 3-TMA-Pb are narrower than those of 2-FMA-Pb and 3-FMA-Pb, indicating their higher crystallinity (Figure S9 and Table S2 in the Supporting Information). Also, the grazing incidence wide-angle X-ray scattering (GIWAXS) measurements were performed on these films (Figure S10 in the Supporting Information). It can be observed that all these films exhibit sharp diffraction spots at the q_z direction, indicating the same lattice orientation along the out-of-plane direction of the film. Further characterization of the perovskite films was performed using UV−vis absorption spectroscopy. Figure 1c reveals that all films display a single absorption peak centered around 500 nm, confirming their pure 2D layered structure. The subtle differences in the band gaps are principally caused by spacer-modulated quantum confinement effects, where decreased organic layer thickness and reduced dielectric mismatch cooperatively decrease carrier localization (Figure S11 in the Supporting Information).[41] Photoluminescence (PL) spectra were also measured under 450 nm laser excitation, as shown in Figure 1d. The 2-TMA-Pb and 3-TMA-Pb films exhibit PL peaks at approximately 524 nm, while the 2-FMA-Pb and 3-FMA-Pb films show peaks at 511 and 513 nm, respectively. The FWHM of the PL spectra for 2-TMA-Pb and 3-TMA-Pb is relatively narrower, indicating superior crystallinity compared to their furan-based counterparts (Table S2). To further evaluate the film morphology, scanning electron microscopy (SEM) was conducted, and the top-view images are presented in Figure 1e and Figures S12 and S13 in the Supporting Information. The 2-TMA-Pb film exhibits minor surface irregularities, including small voids and protrusions, potentially hindering carrier transport. In contrast, the 3-TMA-Pb film displays a smooth and uniform surface, which is beneficial to the transport of carriers, contributing to the superior photodetection performance. On the other hand, both 2-FMA-Pb and 3-FMA-Pb films show significant voids, which can possibly act as recombination centers, adversely affecting device performance. Collectively, these experimental results confirm the successful formation of pure 2D layered perovskites, with 2-TMA-Pb and 3-TMA-Pb films demonstrating superior crystallinity and morphological quality.

As previously discussed, the properties and stability of the RP perovskites are jointly influenced by two key interactions: (1) the interaction between organic spacer layers and inorganic PbI_6 slabs and (2) the interaction between adjacent organic layers. To gain a deeper understanding of how heteroatoms regulate these interactions, we first synthesized single crystals of 2-TMA-Pb and 3-TMA-Pb using a slow cooling crystallization process. Single-crystal X-ray diffraction was then performed to determine their precise crystal structures. The average R factors for both structures were below 4.5%, ensuring the reliability of the structural data for subsequent analysis (Figure S15 and Table S3 in the Supporting Information). Also, the XRD patterns of single crystals for 2-TMA-Pb and 3-TMA-Pb were measured to compare with the corresponding XRD patterns of films, confirming the consistent structure in both crystals and films (Figure S14 in the Supporting Information). Key structural parameters are presented in Figure 2a,b, with the following notable features:

i. Spacer skeleton length: The lengths of the 2-TMA and 3-TMA spacer skeletons are nearly identical, measuring ∼4.393 and ∼4.433 Å, respectively, with 3-TMA being slightly longer.

ii. Inorganic layer spacing: The spacing between adjacent PbI_6 slabs in 2-TMA-Pb (14.519 Å) is significantly larger than that in 3-TMA-Pb (14.129 Å).

iii. S···S Interactions: The minimum distance between sulfur (S) atoms in adjacent organic layers is 3.63 Å, which falls within the range of S···S interactions (typically <3.8 Å), as illustrated in Figure 2a.[27,42,43]

These structural features reveal that the shorter inorganic layer spacing in 3-TMA-Pb, despite its slightly longer spacer skeleton, is attributed to enhanced organic layer-to-layer interactions mediated by S···S interactions. Additionally, the S···π interactions, commonly observed in similar configurations, may further contribute to this strengthened interaction (Figure 2f).[44−46] Another critical structural parameter is the penetration depth (d_p), defined as the distance between the nitrogen (N) atom plane of the spacer and the axial iodine(I) atom plane of the PbI_6 slabs. This parameter reflects the steric interaction between the organic spacers and the inorganic framework, with a larger d_p indicating stronger interactions.[16,47,48] As shown in Figure 2b, the d_p of 2-TMA-Pb (∼0.526 Å) is slightly greater than that of 3-TMA-Pb (∼0.492 Å), suggesting that 2-TMA spacers exhibit stronger interactions with the PbI_6 slabs compared to 3-TMA spacers. To further investigate the intermolecular interactions within the organic layers, we conducted a Hirschfeld surface analysis, which provides a visual representation of molecular electrostatic interactions.[49] As shown in Figure 2c,d, 3-TMA-Pb exhibits a significant S···S interaction contribution (∼4.2%), whereas no such interactions are observed in 2-TMA-Pb. This finding underscores the stronger interlayer interactions in 3-TMA-Pb, which are further corroborated by its superior thermal stability. In addition, the Hirschfeld surface analysis related to S···π and π···π interactions is presented in Figure S16 in the Supporting Information. Thermogravimetric analysis (TGA) results (Figure 2e) reveal that 3-TMA-Pb begins to decompose at 234 °C under a heating rate of 10 °C/min in a nitrogen atmosphere, compared to 215 °C for 2-TMA-Pb. This enhanced thermal stability can be attributed to the reinforced organic layer-to-layer interactions in 3-TMA-Pb.[33,50] These results demonstrate that the position of the S atom plays a critical role in modulating the internal interactions within RP perovskites. Specifically, the S atom in 2-TMA preferentially interacts with the PbI_6 slabs, while in 3-TMA, it strengthens van der Waals interactions between organic layers.

To further probe the internal interactions in 2-FMA-Pb, 3-FMA-Pb, 2-TMA-Pb, and 3-TMA-Pb, we performed X-ray photoelectron spectroscopy (XPS). The results, calibrated using the C 1s spectra, are presented in Figure 2g and Figures S17−S19 in the Supporting Information. The Pb 4f spectra of these samples exhibit two main peaks corresponding to Pb $4f_{7/2}$ and Pb $4f_{5/2}$. As is well-known, the binding energy (E_B) is highly dependent on the chemical environment. For the 2-TMA-Pb sample, the Pb $4f_{7/2}$ and Pb $4f_{5/2}$ peaks are located at 138.3 and 143.2 eV, respectively, which are slightly lower than those of the 3-TMA-Pb sample (138.4 and 143.3 eV). This indicates a

https://doi.org/10.1021/acsnano.5c09104
ACS Nano 2025, 19, 41498−41508

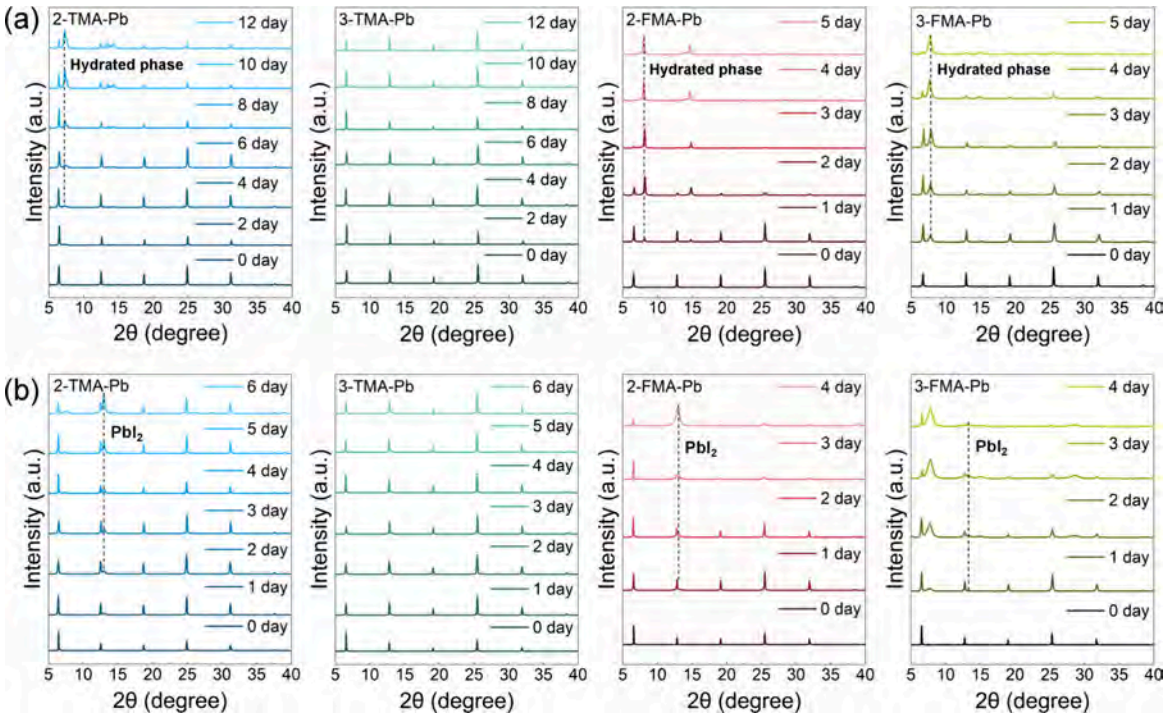

Figure 3. (a) Air stability test under 40% ± 5% RH at room temperature monitored using XRD measurements for 2-TMA-Pb, 3-TMA-Pb, 2-FMA-Pb, and 3-FMA-Pb perovskite films. (b) Thermal stability test at 75 °C ± 5° under RH of 40% ± 5% environments for 2-TMA-Pb, 3-TMA-Pb, 2-FMA-Pb, and 3-FMA-Pb perovskite films.

stronger interaction between the 2-TMA spacer and the PbI_6 slabs, consistent with the single-crystal structural analysis. In contrast, the E_B values for Pb $4f_{7/2}$ and Pb $4f_{5/2}$ in 2-FMA-Pb (138.6 and 143.5 eV) and 3-FMA-Pb (138.7 and 143.6 eV) are significantly higher, suggesting weaker interactions between the furan-based spacers and the inorganic sheets. This phenomenon can likely be attributed to the lower aromaticity of the furan molecule compared to thiophene.[37] A similar trend is observed in the XPS spectra of iodine(I), as shown in Figure 2g. Furthermore, the magnified view of the (002) peaks in the XRD patterns (Figure 2h) provides additional insights into the interlayer distances between PbI_6 layers. The inorganic layer spacing follows a decreasing trend: 2-TMA-Pb > 2-FMA-Pb > 3-FMA-Pb > 3-TMA-Pb. Structurally, the 2-FMA spacer is shorter than the 2-TMA spacer due to the shorter C−O bond length compared to the C−S bond length, resulting in a smaller spacing between adjacent inorganic layers in 2-FMA-Pb. Notably, when the spacer changes from 2-TMA to 3-TMA, the inorganic layer spacing of the corresponding RP perovskite significantly narrows, as evidenced by the shift of the (002) peak from 6.43 to 6.62°. This substantial shift is attributed to the enhanced organic layer-to-layer interactions, as demonstrated by single-crystal structural analysis. However, the (002) peak position of 3-FMA-Pb (2θ = 6.64°) is only slightly higher than that of 2-FMA-Pb (2θ = 6.60°), indicating that the oxygen (O) atom in furan does not enhance the binding strength between organic layers as effectively as the sulfur (S) atom in thiophene. This difference may arise from the smaller atomic size of oxygen compared to sulfur, limiting its ability to participate in strong intermolecular interactions. To further explore the interaction between organic layers, we calculated charge density difference maps for these RP perovskites. As illustrated in Figure S20 of the Supporting Information, the resulting isosurfaces show distinct electron accumulation (green) and depletion (red) regions. These maps reveal the charge transfer between adjacent organic layers in 3-TMA-Pb while showing no comparable electron redistribution in 3-FMA-Pb, 2-TMA-Pb, or 2-FMA-Pb. This finding provides direct evidence of S···S intermolecular interactions within the thiophene-based 3-TMA-Pb structure, conspicuously absent in its furan-containing counterpart.

To quantitatively evaluate the energy contributions of S···S interactions in 3-TMA-Pb (and at the same time compare them with the O···O interactions in 3-FMA-Pb), we performed crystal orbital Hamilton population (COHP) analyses between adjacent S atoms (or O atoms). This method can directly quantify interaction strengths between the atoms. Notably, the states below the Fermi level for the nearest S···S and O···O atom pairs correspond to bonding states, which stabilize their respective structures. The calculated integrated COHP (ICOHP) values are labeled in Figure S21 in the Supporting Information. The stronger S···S interactions, evidenced by their more negative ICOHP value (−0.03 eV compared to −0.005 eV for O···O), contribute approximately 6-fold greater bonding energy per interaction pair, highlighting stronger electronic cloud overlap between organic layers in 3-TMA-Pb, which collectively enhances the overall lattice stabilization. The marked contrast between 3-TMA-Pb and 3-FMA-Pb highlights the critical role of heteroatom selection (S vs O) in governing interlayer electronic coupling, demonstrating the superior charge mediation capability of thiophene moieties compared to furan systems.

To further investigate the influence of internal interactions on the stability of these RP perovskites, we systematically evaluated their stability under ambient air and elevated temperature conditions. The structural changes were monitored using time-dependent X-ray diffraction (XRD) measurements (Figures S23 and S24 in Supporting Information). For the air stability tests, the perovskite films were exposed to a controlled environment

https://doi.org/10.1021/acsnano.5c09104
ACS Nano 2025, 19, 41498−41508

with a relative humidity (RH) of 40% ± 5% and a temperature of 25 °C. As shown in Figure 3a, after 5 days, the primary diffraction peaks of 2-FMA-Pb and 3-FMA-Pb films disappeared, accompanied by the emergence of new peaks in the low-angle region (5−10°). Notably, no PbI_2 peaks were observed, indicating that the degradation mechanism differs from simple decomposition into PbI_2. According to previous studies, low-angle peaks in this range indicate hydrated species formation resulting from the intrusion of H_2O molecules into the perovskite framework. These water molecules compete with PbI_2 to bind with the NH_3^+ groups of the organic spacers, leading to structural collapse.[51,52] The rapid degradation of 2-FMA-Pb and 3-FMA-Pb can be attributed to the weak interactions between the organic spacers and the inorganic PbI_6 lattices, which are insufficient to prevent water molecule penetration. In contrast, 2-TMA-Pb and 3-TMA-Pb films exhibited significantly better air stability, with no notable changes observed after 6 days. This enhanced stability directly results from the stronger interactions between the organic spacers and the inorganic layers. After 12 days, the 2-TMA-Pb film began to show signs of hydration, as evidenced by the appearance of low-angle peaks, while the 3-TMA-Pb film retained its original diffraction pattern, demonstrating superior stability. The better stability of 3-TMA-Pb arises from the robust interactions between the organic spacers and the inorganic PbI_6 slabs and the strengthened van der Waals forces within the organic layers themselves. In addition, it is noteworthy that after 1 month of storage in air, no noticeable impurity peak appeared for the 3-TMA-Pb film (Figure S22 in the Supporting Information). Subsequently, we evaluated the thermal stability of these films by placing them on a hot plate at 75 °C ± 5 °C under the same RH conditions (40% ± 5%). The results, shown in Figure 3b, reveal that under high-temperature conditions, the diffraction peaks corresponding to PbI_2 gradually emerged for both 2-FMA-Pb and 3-FMA-Pb films, and their primary perovskite peaks weakened significantly after 4 days. A similar trend was observed for the 2-TMA-Pb film, although it exhibited better thermal degradation resistance than the furan-based samples. Remarkably, the 3-TMA-Pb film demonstrated the highest thermal stability, with minimal structural changes even after 6 days. These thermal stability results align with the air stability observations, further underscoring the critical role of internal interactions in determining the stability of RP perovskites. Specifically, the combined effects of strong organic−inorganic interactions and enhanced interlayer van der Waals forces are key to achieving superior stability in these materials.

Based on the comprehensive analysis above, the relationship between the stability and internal interactions of these four RP perovskites is summarized in the schematic diagram shown in Figure 4. It is evident that 2-FMA-Pb and 3-FMA-Pb exhibit relatively low stability due to their weak internal interactions, including both the organic−inorganic layer interactions and the interlayer interactions between organic spacers. In contrast, 2-TMA-Pb demonstrates improved stability compared to furan-based counterparts, primarily due to its stronger organic−inorganic interactions. However, its stability is still limited by the weaker interlayer interactions between organic spacers. Remarkably, 3-TMA-Pb, which benefits from robust organic−inorganic interactions and enhanced interlayer van der Waals forces, exhibits the highest stability among the four perovskites. Table S4 in the Supporting Information summarizes the reported thiophene-based spacers, highlighting the advantage

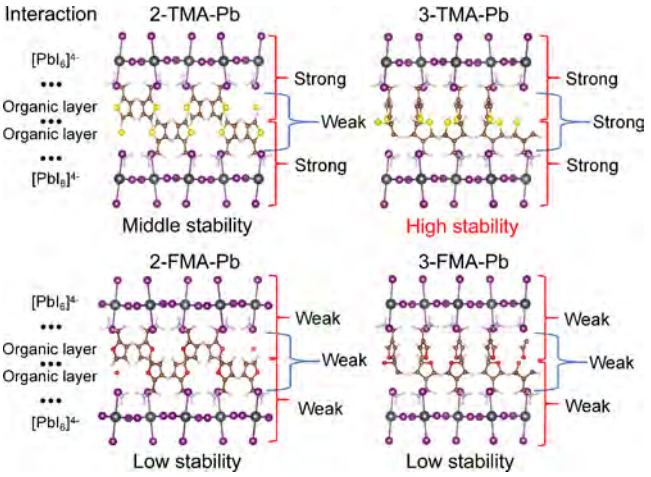

Figure 4. Schematic diagram of the relationship between the stability and internal interaction for 2-TMA-Pb, 3-TMA-Pb, 2-FMA-Pb, and 3-FMA-Pb perovskite films.

of 3-TMA in enhancing the internal interactions within RP perovskites.

To further explore the photoelectric properties of these perovskites, we fabricated photodetectors based on 2-TMA-Pb, 3-TMA-Pb, 2-FMA-Pb, and 3-FMA-Pb films. As illustrated in Figure 5a, a coplanar device structure was employed, with Au electrodes deposited onto the perovskite films. A 450 nm laser was used to illuminate the active area of the photodetectors from the top. The current−time (I−t) curves, measured under a light intensity of 45.5 mW/cm^2 at a bias of 1.5 V, exhibit stable and reversible on/off switching characteristics, as shown in Figure 5b. In detail, the 3-TMA-Pb and 2-TMA-Pb detectors exhibited relatively high photocurrent values of over 6.5 and 5.0 nA, respectively, while the 2-FMA-Pb and 3-FMA-Pb devices showed lower responses, with photocurrent values around 1 nA. The dark current of all devices remained at a similar level, approximately 10^{-2} nA, and the corresponding on/off ratios are calculated as 1.9×10^2, 1.4×10^2, $2.1 \times 10,^1$ and 6.2×10^1 for 2-TMA-Pb, 3-TMA-Pb, 2-FMA-Pb, and 3-FMA-Pb devices, respectively. These parameters are summarized in Table S5 in the Supporting Information. The current−voltage (I−V) curves were also measured under varying light intensities and dark conditions (see Figure S25 in the Supporting Information). All I−V curves display linear behavior, confirming the formation of ohmic contacts between the Au electrodes and the perovskite films. Under the same light intensity (45.5 mW/cm^2), the photodetector based on the 3-TMA-Pb film demonstrates the highest photocurrent (Figure 5c), which can be attributed to its superior film quality and the large dipole moment of the 3-TMA spacer. Furthermore, the I−T measurements reveal a linear increase in photocurrent with increasing light intensity, a phenomenon related to the generation, trapping, and recombination dynamics of electron−hole pairs in semiconductor devices. We calculated the linear dynamic range (LDR) using the equation LDR = 20 log(P_{upper}/P_{lower}), where P_{lower} and P_{upper} represent the lowest and highest light intensities, respectively. Our perovskite devices display an obvious linear response from 0.00455 to 45.536 mW over cm^2, indicating a large LDR of 80 dB. To quantitatively evaluate the photodetection performance, three key parameters were calculated: responsivity (R), detectivity (D^*), and external quantum efficiency (EQE). These parameters are defined by the following equations: R =

https://doi.org/10.1021/acsnano.5c09104
ACS Nano 2025, 19, 41498−41508

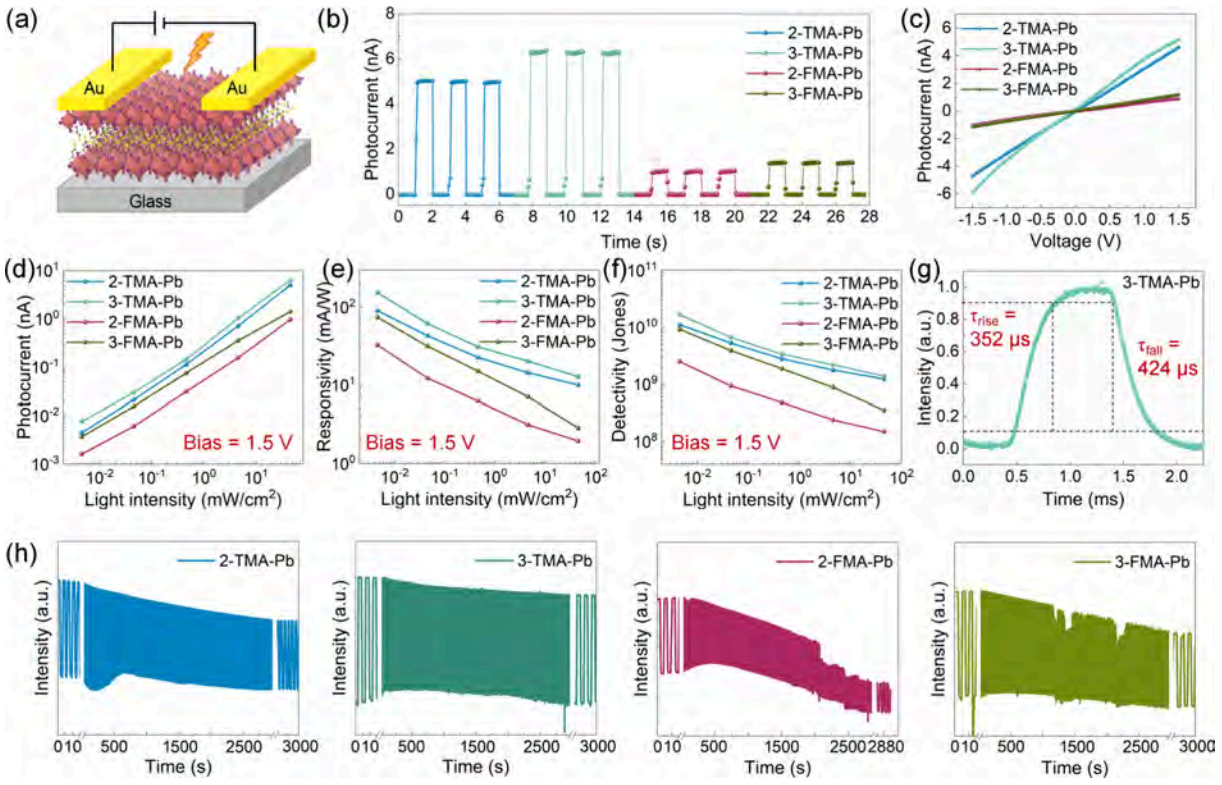

Figure 5. (a) Structure of a perovskite photodetector. (b) On−off switching curves of 2-TMA-Pb, 3-TMA-Pb, 2-FMA-Pb, and 3-FMA-Pb perovskite photodetectors, which are tested under a light intensity of 45.5 mW/cm^2 at 1.5 V. (c) I−V curves of these perovskite photodetectors under a light intensity of 45.5 mW/cm^2. (d−f) Relationship curves of light intensity with photocurrent, responsivity, and detectivity, respectively, at 1.5 V. (g) Determination of the rise and fall times of the 3-TMA-Pb photodetector at a bias of 1.5 V. (h) Long-time operation stability test of these four perovskite photodetectors under a light intensity of 22.7 mW/cm^2 at 1.5 V.

Table 1. Summary of Various Metrics of 2D RP Perovskite Photodetectors[a]

perovskites	bias [V]	λ [nm]	R [mA/W]	D^* [Jones]	rise/decay time [ms]	reference
$(BA)_2PbI_4$	5	white light	3.0	N/A	28.4/27	53
$(OA)_2PbI_4$	5	470	2.89	N/A	200/500	54
$(4FH\text{-}PPH)_2PbI_4$	5	450	168.2	[b] 1.9×10^{10}	43/46	55
(R)-$\alpha(PEA)_2PbI_4$	3	520	600	[c] 3.06×10^{11}	22/34	56
$(PEA)_2PbI_4$ crystal	5	Solar light	5	[c] 1.07×10^{13}	N/A	57
$(3AMPY)EAPb_2Br_7$	10	800	0.01	N/A	N/A	58
$(C_6H_5(CH_2)_3NH_3)_3Pb_2I_7$	5	515	N/A	[b] 1.2×10^{10}	0.85/0.78	59
$(BA)_2(MA)_2Pb_3I_{10}$	2	532	<30	[b] 5×10^{8}	10/10	60
$(C_5H_{11}NH_3)_2(MA)Pb_2I_7$	9.5	600	3.87	[b] 2.92×10^{10}	0.0015/0.0017	61
$(iBA)_2(MA)_3Pb_4I_{13}$	1.5	532	120	N/A	16/15	62
3-TMA$_2$PbI$_4$	1.5	450	153	[c] *1.7×10^{10}*	*0.352/0.424*	*this work*

[a]Note: different formula for calculating detectivity (D^*). [b]$D^* = RS^{1/2}/(2eI_{dark})^{1/2}$, where e is the electronic charge, S is the effective area of the photodetector, R is the responsivity, and I_{dark} is the dark current. [c]$D^* = R(S)^{1/2}/(I_n)^{1/2}$, where S is the effective area of the photodetector, R is the responsivity, and I_n is the noise current.

$I_p - I_d/\Phi S$, $D^* = S^{1/2}/\mathrm{NEP}$ and $\mathrm{EQE} = hcR/e\lambda$, where I_p is the photocurrent, I_d is the dark current, Φ is the light intensity, S is the active area of the photodetector, NEP is the noise equivalent power, h is Planck's constant, c is the speed of light, and λ is the wavelength of the excitation light. The NEP is calculated as $\mathrm{NEP} = I_n/R$, where I_n represents the current noise spectral density, which is shown in Figure S26. As shown in Figure 5d−f and Figure S27 in the Supporting Information, the 3-TMA-Pb photodetector achieves the highest performance metrics, with R = 153.9 mA/W, $D^* = 1.7 \times 10^{10}$ Jones, and EQE = 42.5%. These values significantly surpass those of the 2-TMA-Pb (89.9 mA/W, 1.1×10^{10} Jones and 24.8%), 2-FMA-Pb (32.6 mA/W, 2.5×10^{9} Jones and 9.04%), and 3-FMA-Pb (74.3 mA/W, 9.2×10^{9} Jones and 20.5%) devices. Notably, for the 2-FMA-Pb and 3-FMA-Pb devices, the voids within the films are one of the primary factors affecting their performance because these voids can act as defects, leading to nonradiative recombination of photogenerated carriers, thereby impeding the transport of the charge. By contrast, the improved performance of the 3-TMA-Pb photodetector can be attributed to its good film quality, which facilitates the efficient transport of photogenerated carriers. Additionally, the short inorganic layer spacing and the large dipole moment of the 3-TMA spacer collectively weaken the quantum and dielectric confinement effects, reducing the

https://doi.org/10.1021/acsnano.5c09104
ACS Nano 2025, 19, 41498−41508

exciton binding energy and promoting the separation and transport of electron−hole pairs. Since the photoresponse of detectors varies with wavelength, we measured the spectral response characteristics of 2-TMA-Pb, 3-TMA-Pb, 2-FMA-Pb, and 3-FMA-Pb devices between 400 and 700 nm. As Figure S28 in the Supporting Information shows, these detectors primarily exhibit photoresponse in the wavelength range of 400−520 nm. More specifically, the peak spectral responses of the 2-TMA-Pb and 3-TMA-Pb-based detectors are located near 510 nm, while those of 2-FMA-Pb and 3-FMA-Pb appear around 500 nm, consistent with their respective absorption characteristics. In addition, the 3 dB bandwidth is used to characterize the operating frequency of the detectors. The frequency-dependent response of these devices under excitation ranging from 100 to 10,000 Hz was tested, and the results are presented in Figure S29 in the Supporting Information. The 3-TMA-Pb detector exhibits the highest operating frequency of 3.2 kHz, with the devices based on 2-TMA-Pb, 2-FMA-Pb, and 3-FMA-Pb showing frequencies of 2.5, 2.1, and 2.3 kHz, respectively. Moreover, response speed, characterized by rise time (transition from 10 to 90% of maximum current) and fall time (decay from 90 to 10% of maximum current), represents critical performance metrics for photodetectors. Time-resolved photocurrent measurements with microsecond resolution were conducted on 2-TMA-Pb, 3-TMA-Pb, 2-FMA-Pb, and 3-FMA-Pb devices (Figure 5g and Figure S30, Supporting Information). Due to the weak carrier transport ability, devices based on 2-FMA-Pb and 3-FMA-Pb exhibit prolonged rise times exceeding 450 μs and fall times exceeding 500 μs. In contrast, the 2-TMA-Pb and 3-TMA-Pb photodetectors enable accelerated response, particularly the 3-TMA-Pb detector, which achieves rise and fall times of 352 and 424 μs, respectively, indicating its good optoelectronic performance. Table 1 (Supporting Information) systematically compares key performance metrics between our photodetector and other low-n halide perovskite-based devices, demonstrating our device's great performance. It is noted that the performance of our device is competitive mainly among photodetectors based on n = 1 2D perovskites, but it does not reach the level of the latest reports using high-n 2D perovskites. To further clarify the role of dimensionality, we also fabricated photodetectors based on n = 3 perovskite films. The results confirm that increasing the n value enhances device responsivity, as shown in Figure S31 in the Supporting Information. Nevertheless, although the performance of n = 1 perovskite-based photodetectors is lower than that of their high-n counterparts, they offer distinct advantages in environmental stability, fabrication simplicity—without needing antisolvents or additives—and simplified device architecture. These characteristics make n = 1 2D perovskites particularly attractive for applications requiring high stability and reproducible large-scale fabrication.

In addition to photoelectric performance, the long-term operational stability of perovskite photodetectors under continuous illumination is a critical factor for their practical applications. The studies above have highlighted the significant influence of internal interactions within RP perovskites on their air and thermal stability, suggesting that similar effects may govern their light stability. To explore this, we evaluated the light stability of photodetectors based on 2-TMA-Pb, 3-TMA-Pb, 2-FMA-Pb, and 3-FMA-Pb by continuously recording their current−time (I−t) curves for 3000 s under a light intensity of 22.7 mW/cm^2 at a bias of 1.5 V (Figure 5h). The results reveal that the photocurrent of the 3-TMA-Pb-based device remains nearly constant over time, demonstrating better light stability. This stability is attributed to the strong internal interactions within the 3-TMA-Pb perovskite, which mitigate degradation under illumination. In contrast, the photocurrents of devices based on 2-TMA-Pb, 2-FMA-Pb, and 3-FMA-Pb exhibit significant degradation over time, with the 2-FMA-Pb device showing the most pronounced decline. To evaluate device stability, the devices were stored at room temperature under ambient air (40% ± 5% RH), and their photoresponse was monitored for about 10 days (Figure S32). The 3-TMA-Pb device exhibited minimal degradation, whereas devices with other spacers, especially 2-FMA-Pb and 3-FMA-Pb, showed considerable decline in performance, further confirming the exceptional device-level stability conferred by the 3-TMA spacer. These observations are consistent with the earlier findings on air and thermal stability, further underscoring the pivotal role of internal interactions in determining the overall stability of RP perovskites.

CONCLUSIONS

In summary, we successfully designed and synthesized two 2D RP perovskites, 3-TMA-Pb and 3-FMA-Pb, using 2-TMA-Pb and 2-FMA-Pb as benchmarks, and conducted an in-depth analysis of their internal interactions. Our study highlights the critical role of the type and position of heteroatoms in determining the stability of RP perovskites. Thiophene-based spacers, in particular, demonstrate superior interactions with PbI_6 sheets than furan-based spacers. Notably, the presence of S···S interactions in 3-TMA-Pb enhances the interactions between the organic layers, resulting in the best stability under environmental and thermal conditions among these perovskites. Furthermore, the substantial dipole moment of 3-TMA-Pb leads to improved photodetector performance, achieving a highest responsivity of 153 mA/W and detectivity of 1.7×10^{10} Jones. Our findings provide valuable insights for designing advanced RP perovskites, which are helpful for further development and potential commercialization.

EXPERIMENTAL SECTION

Materials. The methyl alcohol, diethyl ether, tetrahydrofuran, hydriodic acid (57 wt %), *N*,*N*-dimethylformamide (DMF, 99%), and lead(II) iodide (PbI_2, 99.99%) were purchased from Shanghai Aladdin Biochemical Technology Co., Ltd. Thiophen-3-ylmethanamine (98%), furan-3-ylmethanamine (98%), and furan-2-ylmethanamine (98%) were purchased from Bide Pharmatech Co., Ltd. The 2-thiophenemethylammonium iodide (99%) was purchased from Xi'an Polymer Light Technology Corp.

Synthesis of 3-TMAI, 3-FMAI, and 2-FMAI. A solution of thiophen-3-ylmethanamine (2 mmol) in ethanol (1.5 mL) was stirred under ice bath conditions. Then, 1 mL of hydroiodic acid (57 wt % with 1.5% hypophosphorous acid) was added dropwise for about 1 min. After stirring the mixed solution for 3 h at 0 °C and another 3 h at room temperature, diethyl ether was added to the solution, and yellowish crystals appeared. After filtration, the crude was obtained and recrystallized with ethanol and diethyl ether three times. Finally, the pure 3-TMA solids were obtained. The process for synthesizing 3-FMAI and 2-FMAI is similar to the synthesis of 3-TMAI.

Perovskite Precursor Solution Preparation. The preparation of precursor solutions was finished in the N_2-filled glovebox. The precursor of $(3\text{-TMA})_2PbI_4$ was prepared by dissolving PbI_2 (0.8 mmol) and 3-TMAI (1.6 mmol) in a 200 μL DMF solution. The precursor formulations of $(3\text{-FMA})_2PbI_4$, $(2\text{-FMA})_2PbI_4$, and $(2\text{-TMA})_2PbI_4$ are the same as the $(3\text{-TMA})_2PbI_4$ solution. The mixed solution was stirred for 8 h at room temperature before being filtered.

RP Perovskite Film Preparation. The glass substrates were cleaned sequentially with distilled water, acetone, and isopropyl alcohol

https://doi.org/10.1021/acsnano.5c09104
ACS Nano 2025, 19, 41498−41508

three times. Then, these glass substrates were treated with mild oxygen plasma for 5 min. $(3\text{-TMA})_2PbI_4$, $(3\text{-FMA})_2PbI_4$, $(2\text{-TMA})_2PbI_4$, and $(2\text{-FMA})_2PbI_4$ precursor solutions were spin-coated (20 μL) on the top of glasses at 3000 rpm for 30 s, followed by thermal annealing at 100 °C for 10 min, respectively. The entire process was finished in the N_2 environment.

Preparation of Single Crystals of 2-TMA-Pb and 3-TMA-Pb. The perovskite crystals (2-TMA_2PbI_4 and 3-TMA_2PbI_4) mentioned in this article were synthesized by a solution method utilizing hydroiodic acid as the solvent. PbI_2 (0.4 mmol, 0.186 g) and 2-TMA or 3-TMA (0.8 mmol, 0.192 g) were dissolved in HI acid solution (2 mL). Then, the precursor solution was heated and stirred at 80 °C for 2 h. In a quiet environment, the clear pale-yellow solution was gradually cooled to room temperature. During the cooling process, deep-yellow crystals began forming at the vial's bottom. The solution was kept at room temperature for 1 day to facilitate further crystal growth. After that, the solution was gently decanted to isolate the formed crystals, which were then collected via suction filtration. The isolated crystals were washed with diethyl ether and allowed to dry under ambient air.

Device Fabrication. After obtaining $(3\text{-TMA})_2PbI_4$, $(3\text{-FMA})_2PbI_4$, $(2\text{-TMA})_2PbI_4$, and $(2\text{-FMA})_2PbI_4$ RP perovskite films, 60 nm-thick symmetric Au electrodes were evaporated on these perovskite films to configure photodetectors under the assistance of shadow masks. The channel length and width of the photodetectors were 10 and 70 μm, respectively.

Characterizations. The ^1H NMR and ^{13}C NMR spectra were recorded from a Bruker Avance NEO 400 MHz spectrometer. The XRD patterns were acquired using D2 Phaser with Cu Kα radiation, Bruker. The UV−vis absorption spectra were obtained using a Hitachi UH 4150 UV−vis absorption spectrophotometer, and the steady-state photoluminescence (PL) spectra were tested using the photoluminescence system (FLS1000 system). The morphologies of the perovskite films were characterized by SEM (FEI Quanta 450 FEG SEM). The single-crystal structure was determined using the Rigaku X-ray single-crystal diffractometer system. Thermogravimetric analysis (TGA) measurements were performed on a PerkinElmer simultaneous thermal analyzer (STA) 6000. The Thermo Scientific ESCALAB 250Xi system was employed to perform the XPS measurement. The photodetection performance of the fabricated photodetectors was characterized by a standard electrical probe station and an Agilent 4155C semiconductor analyzer (Agilent Technologies, California, USA). A laser with a wavelength of 450 nm was used as the light source for the photodetector measurement, while the power of the incident irradiation was measured using a power meter (PM400, Thorlabs). An attenuator was also employed to tune the irradiation power illuminating the device. All the photodetection performance measurements were conducted in a light-tight environment to minimize external disturbance.

Density Functional Theory Calculation. The geometry optimization and ESP of 2-TMA, 3-TMA, 2-FMA, and 3-FMA spacers were achieved by the B3LYP/6-311G+(d,p) calculations of density functional theory (DFT).[63] The first-principles calculations for perovskite structures, band structures, and COHPs were performed using DFT in the Vienna Ab initio Simulation Package. The convergence criteria for the energy and atomic forces were set to 3×10^{-4} eV and 0.01 eV Å^{-1}, respectively. The Brillouin zone was sampled with $3 \times 3 \times 3$ k-point meshes for structural optimization and denser $7 \times 7 \times 7$ k-point meshes for the electronic and optical properties. The COHP and the ICOHP were calculated by the Local Orbital Basis Suite Toward Electronic-Structure Reconstruction (LOBSTER) program.

ASSOCIATED CONTENT

Supporting Information

The Supporting Information is available free of charge at https://pubs.acs.org/doi/10.1021/acsnano.5c09104.

^1H NMR spectra; ^{13}C NMR spectra; GIWAXS images; SEM images; detailed crystal data; fitted data; and DFT data and device measurements (PDF)

Crystallographic data (CIF)

Crystallographic data (CIF)

Accession Codes

CCDC 2454735 and 2454736 contain supporting crystallographic data for this work. These data can be obtained free of charge from The Cambridge Crystallographic Data Centre via www.ccdc.cam.ac.uk/data_request/cif.

AUTHOR INFORMATION

Corresponding Authors

Zhengxun Lai − *Changsha Semiconductor Technology and Application Innovation Research Institute, College of Semiconductors (College of Integrated Circuits), Hunan University, Changsha 410082, China*; Email: laizhengxun@hnu.edu.cn

Johnny C. Ho − *Department of Materials Science and Engineering and State Key Laboratory of Terahertz and Millimeter Waves, City University of Hong Kong, Hong Kong SAR 999077, China; Shenzhen Research Institute, City University of Hong Kong, Shenzhen 518057, China; Institute for Materials Chemistry and Engineering, Kyushu University, Fukuoka 816 8580, Japan*; orcid.org/0000-0003-3000-8794; Email: johnnyho@cityu.edu.hk

Authors

Yi Shen − *Department of Materials Science and Engineering, City University of Hong Kong, Hong Kong SAR 999077, China*

Siliang Hu − *Department of Materials Science and Engineering, City University of Hong Kong, Hong Kong SAR 999077, China*

Boxiang Gao − *Department of Materials Science and Engineering, City University of Hong Kong, Hong Kong SAR 999077, China*; orcid.org/0000-0001-8422-5941

Yan Yan − *Department of Materials Science and Engineering, City University of Hong Kong, Hong Kong SAR 999077, China*

Haifan Li − *Department of Chemistry, City University of Hong Kong, Hong Kong SAR 999077, China*

Shiyan Shan − *Department of Materials Science and Engineering, City University of Hong Kong, Hong Kong SAR 999077, China*

Jianbo Wu − *Department of Materials Science and Engineering, City University of Hong Kong, Hong Kong SAR 999077, China*

Dong Chen − *Department of Materials Science and Engineering, City University of Hong Kong, Hong Kong SAR 999077, China*

Yuxuan Zhang − *Department of Materials Science and Engineering, City University of Hong Kong, Hong Kong SAR 999077, China*

Dylan Xiangyu Fan − *American International School, Hong Kong SAR 999077, China*

Chun-Yuen Wong − *Department of Chemistry, City University of Hong Kong, Hong Kong SAR 999077, China*; orcid.org/0000-0003-4780-480X

Complete contact information is available at: https://pubs.acs.org/10.1021/acsnano.5c09104

Author Contributions

Y.S. and Z.L. implemented the idea, designed the experiments, analyzed the data, and wrote the manuscript. S.H., B.G., and Y.Y.

https://doi.org/10.1021/acsnano.5c09104
ACS Nano 2025, 19, 41498−41508

contributed to the completion of the XRD and SEM measurements. H.L., S.S., J.W., D.C., Y.Z., and D.X.F. provided helpful advice and assisted in measuring device performance. Z.L., C.-Y.W., and J.C.H. conceived, founded, and managed the project. All authors analyzed and discussed the results, providing input to the manuscript.

Notes

The authors declare no competing financial interest.

ACKNOWLEDGMENTS

This work is supported by a fellowship award from the Research Grants Council of the Hong Kong Special Administrative Region, China (CityU RFS2021-1S04), the Shenzhen Municipality Science and Technology Innovation Commission (Project no. JCYJ20230807114910021), Guangdong Basic and Applied Basic Research Fund (Project no. 2024A1515011922), and the "111 Center" (Project no. B25033).

REFERENCES

(1) Min, H.; Lee, D. Y.; Kim, J.; Kim, G.; Lee, K. S.; Kim, J.; Paik, M. J.; Kim, Y. K.; Kim, K. S.; Kim, M. G.; Shin, T. J.; Seok, S. Il Perovskite solar cells with atomically coherent interlayers on SnO(2) electrodes. *Nature* **2021**, *598*, 444.

(2) Miyata, A.; Mitioglu, A.; Plochocka, P.; Portugall, O.; Wang, J.T.-W.; Stranks, S. D.; Snaith, H. J.; Nicholas, R. J. Direct measurement of the exciton binding energy and effective masses for charge carriers in organic−inorganic tri-halide perovskites. *Nat. Phys.* **2015**, *11*, 582.

(3) Ono, L. K.; Qi, Y.; Liu, S. Progress toward Stable Lead Halide Perovskite Solar Cells. *Joule* **2018**, *2*, 1961.

(4) Yoo, J. J.; Seo, G.; Chua, M. R.; Park, T. G.; Lu, Y.; Rotermund, F.; Kim, Y. K.; Moon, C. S.; Jeon, N. J.; Correa-Baena, J. P.; Bulovic, V.; Shin, S. S.; Bawendi, M. G.; Seo, J. Efficient perovskite solar cells via improved carrier management. *Nature* **2021**, *590*, 587.

(5) Han, Y.; Zhao, H.; Duan, C.; Yang, S.; Yang, Z.; Liu, Z.; Liu, S. Controlled n-Doping in Air-Stable $CsPbI_2Br$ Perovskite Solar Cells with a Record Efficiency of 16.79%. *Adv. Funct. Mater.* **2020**, *30*, No. 1909972.

(6) Zhou, Y.; Zhou, Z.; Chen, M.; Zong, Y.; Huang, J.; Pang, S.; Padture, N. P. Doping and alloying for improved perovskite solar cells. *J. Mater. Chem. A* **2016**, *4*, 17623.

(7) Sun, Y.; Ge, L.; Dai, L.; Cho, C.; Ferrer Orri, J.; Ji, K.; Zelewski, S. J.; Liu, Y.; Mirabelli, A. J.; Zhang, Y.; Huang, J. Y.; Wang, Y.; Gong, K.; Lai, M. C.; Zhang, L.; Yang, D.; Lin, J.; Tennyson, E. M.; Ducati, C.; Stranks, S. D.; Cui, L. S.; Greenham, N. C. Bright and stable perovskite light-emitting diodes in the near-infrared range. *Nature* **2023**, *615*, 830.

(8) Fu, X.; Wang, M.; Jiang, Y.; Guo, X.; Zhao, X.; Sun, C.; Zhang, L.; Wei, K.; Hsu, H. Y.; Yuan, M. Mixed-Halide Perovskites with Halogen Bond Induced Interlayer Locking Structure for Stable Pure-Red PeLEDs. *Nano Lett.* **2023**, *23*, 6465.

(9) Li, W.; Wu, Q.; Lu, L.; Tian, Y.; Luo, H.; Yun, Y.; Jiang, S.; Chen, M.; Li, C. Molecular engineering for sensitive, fast and stable quasi-two-dimensional perovskite photodetectors. *J. Mater. Chem. C* **2023**, *11*, 3314.

(10) Liu, L.; Liu, S.-Y.; Shi, Y.; Fang, C.-L.; Zhao, S.; Shen, H.-Y.; Chen, M.-X.; Wang, Z.-J.; Ma, Y.; Liu, Y.; Feng, Y.; Tang, J.; Ye, H.-Y.; Niu, G. Anti-perovskites with long carrier lifetime for ultralow dose and stable X-ray detection. *Nat. Photonics* **2024**, *18*, 990.

(11) Tian, W.; Zhou, H.; Li, L. Hybrid Organic-Inorganic Perovskite Photodetectors. *Small* **2017**, *13*, No. 1702107.

(12) Fan, X.; Hong, E.; Wang, P.; Fang, X. Controlled Growth of 2D-3D Perovskite Lateral Heterostructures for Wavelength-Tunable Light Communication. *Adv. Funct. Mater.* **2024**, *35*, No. 2415491.

(13) Deng, M.; Fang, X. 2D Perovskite Oxides toward High-Performance Ultraviolet Photodetection. *Acc. Mater. Res.* **2025**, *6*, 615.

(14) Kim, J. H.; Oh, C. M.; Hwang, I. W.; Park, K.; Lee, K. Organic Surface Doping for High-Performance Perovskite Transistors. *Adv. Funct. Mater.* **2025**, *35*, No. 2411836.

(15) Feng, G.; Loi, H. L.; Wang, T.; Deng, W.; Guan, Z.; Wei, Q.; He, J.; Li, M.; Lee, C. S.; Wang, J.; Zhang, Q.; Yan, F. A-Site Engineering with Thiophene-Based Ammonium for High-Efficiency 2D/3D Tin Halide Perovskite Solar Cells. *Angew. Chem., Int. Ed.* **2025**, *64*, No. e202413584.

(16) Wang, S.; Mandal, M.; Zhang, H.; Breiby, D. W.; Yildiz, O.; Ling, Z.; Floudas, G.; Bonn, M.; Andrienko, D.; Wang, H. I.; Blom, P. W. M.; Pisula, W.; Marszalek, T. Odd-Even Alkyl Chain Effects on the Structure and Charge Carrier Transport of Two-Dimensional Sn-Based Perovskite Semiconductors. *J. Am. Chem. Soc.* **2024**, *146*, 19128.

(17) Leijtens, T.; Eperon, G. E.; Noel, N. K.; Habisreutinger, S. N.; Petrozza, A.; Snaith, H. J. Stability of Metal Halide Perovskite Solar Cells. *Adv. Energy Mater.* **2015**, *5*, No. 1500963.

(18) Matteocci, F.; Cinà, L.; Lamanna, E.; Cacovich, S.; Divitini, G.; Midgley, P. A.; Ducati, C.; Di Carlo, A. Encapsulation for long-term stability enhancement of perovskite solar cells. *Nano Energy* **2016**, *30*, 162.

(19) Miyano, K.; Yanagida, M.; Tripathi, N.; Shirai, Y. Hysteresis, Stability, and Ion Migration in Lead Halide Perovskite Photovoltaics. *J. Phys. Chem. Lett.* **2016**, *7*, 2240.

(20) Smith, I. C.; Hoke, E. T.; Solis-Ibarra, D.; McGehee, M. D.; Karunadasa, H. I. A layered hybrid perovskite solar-cell absorber with enhanced moisture stability. *Angew. Chem., Int. Ed.* **2014**, *53*, 11232.

(21) Gong, J.; Hao, M.; Zhang, Y.; Liu, M.; Zhou, Y. Layered 2D Halide Perovskites beyond the Ruddlesden-Popper Phase: Tailored Interlayer Chemistries for High-Performance Solar Cells. *Angew. Chem., Int. Ed.* **2022**, *61*, No. e202112022.

(22) Liu, Y.; Yuan, S.; Zheng, H.; Wu, M.; Zhang, S.; Lan, J.; Li, W.; Fan, J. Structurally Dimensional Engineering in Perovskite Photovoltaics. *Adv. Energy Mater.* **2023**, *13*, No. 2300188.

(23) Katan, C.; Mercier, N.; Even, J. Quantum and Dielectric Confinement Effects in Lower-Dimensional Hybrid Perovskite Semiconductors. *Chem. Rev.* **2019**, *119*, 3140.

(24) Muljarov, E. A.; Tikhodeev, S. G.; Gippius, N. A.; Ishihara, T. Excitons in self-organized semiconductor/insulator superlattices: PbI-based perovskite compounds. *Phys. Rev. B Condens. Matter* **1995**, *51*, 14370.

(25) Fu, W.; Liu, H.; Shi, X.; Zuo, L.; Li, X.; Jen, A. K. Y. Tailoring the Functionality of Organic Spacer Cations for Efficient and Stable Quasi-2D Perovskite Solar Cells. *Adv. Funct. Mater.* **2019**, *29*, No. 1900221.

(26) Li, Q.; Dong, Y.; Lv, G.; Liu, T.; Lu, D.; Zheng, N.; Dong, X.; Xu, Z.; Xie, Z.; Liu, Y. Fluorinated Aromatic Formamidinium Spacers Boost Efficiency of Layered Ruddlesden−Popper Perovskite Solar Cells. *ACS Energy Lett.* **2021**, *6*, 2072.

(27) Ren, H.; Yu, S.; Chao, L.; Xia, Y.; Sun, Y.; Zuo, S.; Li, F.; Niu, T.; Yang, Y.; Ju, H.; Li, B.; Du, H.; Gao, X.; Zhang, J.; Wang, J.; Zhang, L.; Chen, Y.; Huang, W. Efficient and stable Ruddlesden−Popper perovskite solar cell with tailored interlayer molecular interaction. *Nat. Photonics* **2020**, *14*, 154.

(28) Fang, Z.; Wang, G.; Guan, C.; Zhang, J.; Xiang, Q. Reducing Dielectric Confinement Effect Enhances Carrier Separation in Two-Dimensional Hybrid Perovskite Photocatalysts. *Angew. Chem., Int. Ed.* **2024**, *63*, No. e202411219.

(29) Qiu, Y.; Liang, J.; Zhang, Z.; Deng, Z.; Xu, H.; He, M.; Wang, J.; Yang, Y.; Kong, L.; Chen, C.-C. Tuning the Interfacial Dipole Moment of Spacer Cations for Charge Extraction in Efficient and Ultrastable Perovskite Solar Cells. *J. Phys. Chem. C* **2021**, *125*, 1256.

(30) Zhang, F.; Kim, D. H.; Lu, H.; Park, J. S.; Larson, B. W.; Hu, J.; Gao, L.; Xiao, C.; Reid, O. G.; Chen, X.; Zhao, Q.; Ndione, P. F.; Berry, J. J.; You, W.; Walsh, A.; Beard, M. C.; Zhu, K. Enhanced Charge Transport in 2D Perovskites via Fluorination of Organic Cation. *J. Am. Chem. Soc.* **2019**, *141*, 5972.

(31) Zhang, Y.; Chen, M.; He, T.; Chen, H.; Zhang, Z.; Wang, H.; Lu, H.; Ling, Q.; Hu, Z.; Liu, Y.; Chen, Y.; Long, G. Highly Efficient and Stable FA-Based Quasi-2D Ruddlesden-Popper Perovskite Solar Cells

https://doi.org/10.1021/acsnano.5c09104
ACS Nano 2025, 19, 41498−41508

by the Incorporation of beta-Fluorophenylethanamine Cations. *Adv. Mater.* **2023**, *35*, No. 2210836.
(32) Yan, Y.; Yu, S.; Honarfar, A.; Pullerits, T.; Zheng, K.; Liang, Z. Benefiting from Spontaneously Generated 2D/3D Bulk-Heterojunctions in Ruddlesden-Popper Perovskite by Incorporation of S-Bearing Spacer Cation. *Adv. Sci.* **2019**, *6*, No. 1900548.
(33) Li, H.; Song, J.; Pan, W.; Xu, D.; Zhu, W. A.; Wei, H.; Yang, B. Sensitive and Stable 2D Perovskite Single-Crystal X-ray Detectors Enabled by a Supramolecular Anchor. *Adv. Mater.* **2020**, *32*, No. 2003790.
(34) Gao, Y.; Dong, X.; Liu, Y. Recent Progress of Layered Perovskite Solar Cells Incorporating Aromatic Spacers. *Nano-Micro Lett.* **2023**, *15*, 169.
(35) Lai, H.; Kan, B.; Liu, T.; Zheng, N.; Xie, Z.; Zhou, T.; Wan, X.; Zhang, X.; Liu, Y.; Chen, Y. Two-Dimensional Ruddlesden-Popper Perovskite with Nanorod-like Morphology for Solar Cells with Efficiency Exceeding 15. *J. Am. Chem. Soc.* **2018**, *140*, 11639.
(36) Ni, C.; Huang, Y.; Zeng, T.; Chen, D.; Chen, H.; Wei, M.; Johnston, A.; Proppe, A. H.; Ning, Z.; Sargent, E. H.; Hu, P.; Yang, Z. Thiophene Cation Intercalation to Improve Band-Edge Integrity in Reduced-Dimensional Perovskites. *Angew. Chem., Int. Ed.* **2020**, *59*, 13977.
(37) Wang, R.; Dong, X.; Ling, Q.; Fu, Q.; Hu, Z.; Xu, Z.; Zhang, H.; Li, Q.; Liu, Y. Spacer Engineering for 2D Ruddlesden−Popper Perovskites with an Ultralong Carrier Lifetime of Over 18 μs Enable Efficient Solar Cells. *ACS Energy Lett.* **2022**, *7*, 3656.
(38) Zheng, Y.; Chen, S.-C.; Ma, Y.; Zheng, Q. Furfurylammonium as a Spacer for Efficient 2D Ruddlesden−Popper Perovskite Solar Cells. *Sol. RRL* **2022**, *6*, No. 2200221.
(39) Fu, Q.; Chen, M.; Li, Q.; Liu, H.; Wang, R.; Liu, Y. Selenophene-Based 2D Ruddlesden-Popper Perovskite Solar Cells with an Efficiency Exceeding 19. *J. Am. Chem. Soc.* **2023**, *145*, 21687.
(40) Pariari, D.; Mehta, S.; Mandal, S.; Mahata, A.; Pramanik, T.; Kamilya, S.; Vidhan, A.; Guru Row, T. N.; Santra, P. K.; Sarkar, S. K.; De Angelis, F.; Mondal, A.; Sarma, D. D. Realizing the Lowest Bandgap and Exciton Binding Energy in a Two-Dimensional Lead Halide System. *J. Am. Chem. Soc.* **2023**, *145*, 15896.
(41) Wang, S.; Chen, Z.; Zhao, G.; Wang, F. Quantum confinement effect on the electronic and optical properties of two-dimensional halide perovskites. *Comput. Mater. Sci.* **2023**, *230*, No. 112524.
(42) Zhang, L.; Qi, G.; Zhang, Y.; Wu, H.; Xu, X.; Zhou, G.; Zhu, H.; Li, X.; Wu, G.; Chen, H. Intermolecular interaction assisted fabrication of Dion-Jacobson perovskite film with promoted photovoltaic property. *Chem. Eng. J.* **2023**, *451*, No. 138654.
(43) Steudel, R. Properties of Sulfur-Sulfur Bonds. *Angew. Chem., Int. Ed.* **1975**, *14*, 655.
(44) Luo, W.; Kim, S.; Lempesis, N.; Merten, L.; Kneschaurek, E.; Dankl, M.; Carnevali, V.; Agosta, L.; Slama, V.; VanOrman, Z.; Siczek, M.; Bury, W.; Gallant, B.; Kubicki, D. J.; Zalibera, M.; Piveteau, L.; Deconinck, M.; Guerrero-León, L. A.; Frei, A. T.; Gaina, P. A.; Carteau, E.; Zimmermann, P.; Hinderhofer, A.; Schreiber, F.; Moser, J. E.; Vaynzof, Y.; Feldmann, S.; Seo, J. Y.; Rothlisberger, U.; Milić, J. V. From Chalcogen Bonding to S−π Interactions in Hybrid Perovskite Photovoltaics. *Adv. Sci.* **2024**, *11*, No. 2405622.
(45) Pascoe, D. J.; Ling, K. B.; Cockroft, S. L. The Origin of Chalcogen-Bonding Interactions. *J. Am. Chem. Soc.* **2017**, *139*, 15160.
(46) Vogel, L.; Wonner, P.; Huber, S. M. Chalcogen Bonding: An Overview. *Angew. Chem., Int. Ed.* **2019**, *58*, 1880.
(47) Li, W.; Feng, X.; Guo, K.; Pan, W.; Li, M.; Liu, L.; Song, J.; He, Y.; Wei, H. Prominent Free Charges Tunneling Through Organic Interlayer of 2D Perovskites. *Adv. Mater.* **2023**, *35*, No. 2211808.
(48) Wang, W.; Liu, C. D.; Fan, C. C.; Fu, X. B.; Jing, C. Q.; Jin, M. L.; You, Y. M.; Zhang, W. Rational Design of 2D Metal Halide Perovskites with Low Congruent Melting Temperature and Large Melt-Processable Window. *J. Am. Chem. Soc.* **2024**, *146*, 9272.
(49) Spackman, P. R.; Turner, M. J.; McKinnon, J. J.; Wolff, S. K.; Grimwood, D. J.; Jayatilaka, D.; Spackman, M. A. CrystalExplorer: a program for Hirshfeld surface analysis, visualization and quantitative analysis of molecular crystals. *J. Appl. Crystallogr.* **2021**, *54*, 1006.
(50) Zhong, H.; You, S.; Wu, J.; Zhu, Z. K.; Yu, P.; Li, H.; Wu, Z. Y.; Li, Y.; Guan, Q.; Dai, H.; Qu, C.; Wang, J.; Chen, S.; Ji, C.; Luo, J. Multiple Interlayer Interactions Enable Highly Stable X-ray Detection in 2D Hybrid Perovskites. *JACS Au* **2024**, *4*, 2393.
(51) Gao, L.; Li, X.; Traore, B.; Zhang, Y.; Fang, J.; Han, Y.; Even, J.; Katan, C.; Zhao, K.; Liu, S.; Kanatzidis, M. G. m-Phenylenediammonium as a New Spacer for Dion-Jacobson Two-Dimensional Perovskites. *J. Am. Chem. Soc.* **2021**, *143*, 12063.
(52) Leguy, A. M. A.; Hu, Y.; Campoy-Quiles, M.; Alonso, M. I.; Weber, O. J.; Azarhoosh, P.; van Schilfgaarde, M.; Weller, M. T.; Bein, T.; Nelson, J.; Docampo, P.; Barnes, P. R. F. Reversible Hydration of CH3NH3PbI3 in Films, Single Crystals, and Solar Cells. *Chem. Mater.* **2015**, *27*, 3397.
(53) Zhou, J.; Chu, Y.; Huang, J. Photodetectors Based on Two-Dimensional Layer-Structured Hybrid Lead Iodide Perovskite Semiconductors. *ACS Appl. Mater. Interfaces* **2016**, *8*, 25660.
(54) Perumallapelli, G. R.; Tsuda, T.; Formanek, P.; Kiriy, N.; Bakulev, V.; Simon, F.; Voit, B.; Mannsfeld, S. C. B.; Kiriy, A. New insights into the structure of two-dimensional lead iodide-based perovskites. *Org. Electron.* **2020**, *87*, No. 105935.
(55) Lu, N.; Gurumallappa, G.; Singh, J.; Chan, K. L.; Tessema, E.; Liu, P. Y.; Mylnahalli Krishnegowda, H.; Chimatahalli Shanthakumar, K.; Ho, J. H.; Chao, Y. C.; Dao, L. G.; Shirsat, S.; Tsai, M. L. Fast, Highly Stable, and Low-Bandgap 2D Halide Perovskite Photodetectors Based on Short-Chained Fluorinated Piperidinium as a Spacer. *ACS Appl. Mater. Interfaces.* **2025**, *17*, 1743.
(56) Wang, J.; Fang, C.; Ma, J.; Wang, S.; Jin, L.; Li, W.; Li, D. Aqueous Synthesis of Low-Dimensional Lead Halide Perovskites for Room-Temperature Circularly Polarized Light Emission and Detection. *ACS Nano* **2019**, *13*, 9473.
(57) Lin, C.-H.; Cheng, B.; Li, T.-Y.; Retamal, J. R. D.; Wei, T.-C.; Fu, H.-C.; Fang, X.; He, J.-H. Orthogonal Lithography for Halide Perovskite Optoelectronic Nanodevices. *ACS Nano* **2018**, *13*, 1168.
(58) Fu, D.; Jia, W.; Wu, S.; Chang, J.; Chen, Z.; Luo, J. Bilayered Dion−Jacobson Hybrid Perovskite Bulk Single Crystals Constructed with Aromatic Diammonium for Ultraviolet−Visible−Near-Infrared Photodetection. *Chem. Mater.* **2023**, *35*, 2541.
(59) Fu, X.; Jiao, S.; Jiang, Y.; Li, L.; Wang, X.; Zhu, C.; Ma, C.; Zhao, H.; Xu, Z.; Liu, Y.; Huang, W.; Zheng, W.; Fan, P.; Jiang, F.; Zhang, D.; Zhu, X.; Wang, X.; Pan, A. Large-Scale Growth of Ultrathin Low-Dimensional Perovskite Nanosheets for High-Detectivity Photodetectors. *ACS Applied Materials & Interfaces.* **2020**, *12*, 2884.
(60) Fu, Q.; Wang, X.; Liu, F.; Dong, Y.; Liu, Z.; Zheng, S.; Chaturvedi, A.; Zhou, J.; Hu, P.; Zhu, Z.; Bo, F.; Long, Y.; Liu, Z. Ultrathin Ruddlesden−Popper Perovskite Heterojunction for Sensitive Photodetection. *Small* **2019**, *15*, No. 1902890.
(61) Han, S.; Wang, P.; Zhang, J.; Liu, X.; Sun, Z.; Huang, X.; Li, L.; Ji, C.; Zhang, W.; Teng, B.; Hu, W.; Hong, M.; Luo, J. Exploring a Polar Two-dimensional Multi-layered Hybrid Perovskite of $(C_5H_{11}NH_3)_2(CH_3NH_3)Pb_2I_7$ for Ultrafast-Responding Photodetection. *Laser Photonics Rev.* **2018**, *12*, No. 1800060.
(62) Dong, R.; Lan, C.; Xu, X.; Liang, X.; Hu, X.; Li, D.; Zhou, Z.; Shu, L.; Yip, S.; Li, C.; Tsang, S.-W.; Ho, J. C. Novel Series of Quasi-2D Ruddlesden−Popper Perovskites Based on Short-Chained Spacer Cation for Enhanced Photodetection. *ACS Applied Materials & Interfaces.* **2018**, *10*, 19019.
(63) Becke, A. D. Density-functional thermochemistry. I. The effect of the exchange-only gradient correction. *J. Chem. Phys.* **1992**, *96*, 2155.

https://doi.org/10.1021/acsnano.5c09104
ACS Nano 2025, 19, 41498−41508